Polar Direct Drive—Proof-of-Principle Experiments on OMEGA and Prospects for Ignition on the National Ignition Facility

Introduction

This article supports the preceding article ("The Saturn Target for Polar Direct Drive on the National Ignition Facility," p. 61) by presenting recent experimental and simulation results indicating that ignition may be feasible on the National Ignition Facility (NIF)[1] using polar direct drive (PDD).[2]

Since the recent suggestion[3] that the PDD option be reconsidered on account of the cost and complexity of rerouting half of the NIF beams, a number of two-dimensional (2-D) hydrodynamic PDD simulations have been reported. Simulations[4,5] of the all-DT capsule design of Refs. 6 and 7 were carried out using the hydrodynamics code *SAGE*, which includes fully self-consistent 3-D ray tracing.[8] These simulations used sets of optimized repointings of the four rings of NIF beams and elliptical far-field focal spots for some rings to increase the drive on the capsule equator. Skupsky *et al*.[2] used the 2-D code *DRACO*[9,10] to examine PDD designs for wetted-foam capsules,[11] which are attractive because of increased laser absorption. They concluded that PDD enhances the capability of the NIF to explore ignition conditions and found that the primary cause of gain reduction was the time-dependent drive deficit on the equator due to target compression.[12] The previous article (p. 61) describes simulations of a new "Saturn" target concept for PDD in which a low-*Z* ring is placed around the capsule in the equatorial plane. The plasma produced around the ring (by a combination of light refracted from the capsule and light directly intercepted by the ring) grows so that, at later times, laser rays that would otherwise miss the critical surface in the equatorial region of the capsule are now refracted by the ring plasma to provide stronger irradiation of this region. With appropriately chosen ring dimensions, the capsule can be driven with a uniformity (~1%) approaching that of a symmetrically driven capsule.

The success of PDD on the NIF depends, to a large extent, on the accuracy with which the drive uniformity resulting from proposed laser-beam repointings can be predicted and diagnosed. Two initial series of PDD experiments have been carried out using the 60-beam OMEGA Laser Facility to address these issues. To approximate the NIF irradiation configuration, 40 OMEGA beams are used to irradiate the capsule, with the 20 beams near the equator omitted from the laser drive (some of these beams are used for backlighting).

The optimum repointings for the experiments were calculated on the basis of numerous 2-D *SAGE* simulations for different combinations of these parameters. In every case, the drive was found to be too low on the equator. The optimum repointings minimized the overall rms nonuniformity in the center-of-mass velocity of the imploding shell at the end of the laser pulse, producing a predicted $\ell = 4$ pattern with the drive low at both the equator and the poles. Both experimental series showed this $\ell = 4$ pattern with the predicted amplitude, confirming the simulations as well as the pointing accuracy and reproducibility of the OMEGA system.

The low drive on the equator can be understood as follows: Since the central portion of the OMEGA on-target beam profile is fairly flat, the intensity incident from a beam with the largest angle (59°) to the vertical is larger at the point on the capsule ($\theta = 59°$) irradiated at normal incidence than at the equator, which sees a flux reduced by cos (31°). Two other factors further reduce the equatorial drive: (a) the absorption falls off as the angle of incidence increases, and (b) once a plasma has formed around the capsule, the energy deposited from obliquely incident rays is spread over a curved path. To provide compensation for all of these factors, the beams aimed at the equator would need more tightly focused spatial profiles (as proposed for the NIF[4,5]).

In the second series of experiments, three Saturn targets were imploded on OMEGA. For these targets, the framed x-ray backlighting results showed a clear $\ell = 2$ drive nonuniformity, with an enhanced drive at the equator that was greater than predicted. These results are very encouraging and suggest that it should be possible to move some of the beam pointings back toward the poles to remove the $\ell = 2$ mode.

This article begins with a description of the initial PDD experiments on OMEGA and their associated modeling. One novel aspect of this modeling is the use of *SAGE*-calculated velocity perturbations at the end of the laser pulse to perturb 2-D *DRACO* simulations that are symmetric until this time. This combines the *SAGE* ray-tracing capability with the burn physics and better implosion hydrodynamics in *DRACO*. These initial experiments are known as "standard-PDD" experiments to distinguish them from the Saturn experiments that are described in the following section. The combined *SAGE*/*DRACO* modeling is then applied to the NIF all-DT Saturn design of the previous article. When the implosion-velocity nonuniformitiy at the end of the laser pulse (~1% rms) is imposed on a uniform *DRACO* simulation at this time, the resulting target gain is close to the gain of 45 that results from a 1-D symmetric calculation.[7] This greatly enhances the prospects of obtaining direct-drive ignition on the NIF using the indirect-drive configuration.

Standard-PDD Experiments on OMEGA

Figure 102.6 shows an Aitoff projection of the OMEGA experimental configuration used to approximate the NIF irradiation configuration. Some of the near-equatorial beams are directed to a gold backlighter foil, viewed by an x-ray framing camera at an angle of 10.8° below the horizontal. Similar 40-beam configurations were first used by Glendinning[13] and Kyrala[14] to diagnose approximately spherical implosions with x-ray backlighting.

The pointings Δr used for the three rings of beams are shown in Fig. 102.7(a). They were verified experimentally by irradiating 4-mm-diam, gold-coated spheres with the repointed beams and comparing x-ray pinhole images with predictions. (This method, applied previously to beams pointed at target chamber center, is described in Ref. 15.) The implosion target is nominally a 20-μm-thick CH shell of 865-μm diameter filled with 15 atm of D_2. The arrows in Fig. 102.7(a) indicate the beam axes. Optimum drive at the equator is obtained by overlapping ring 3 and its lower-hemisphere counterpart on the equator. The beam spatial profile $I(r)$ (including 2-D smoothing by spectral dispersion[16] with 1-THz bandwidth and polarization smoothing[17]) is approximated[18] as a "super-Gaussian" with $I(r) = \exp-(r/r_0)^n$, with r_0 = 380 μm and n = 3.7 [Fig. 102.7(b)]. A significant portion of the laser energy initially misses the target. This is temporary, however, as many of these rays refract through the expanding plasma (see Fig. 102.8), propagating significant distances at densities above quarter-critical $(n_c/4)$ and undergoing significant absorption. Some rays that miss the initial target surface later experience ~50% absorption.

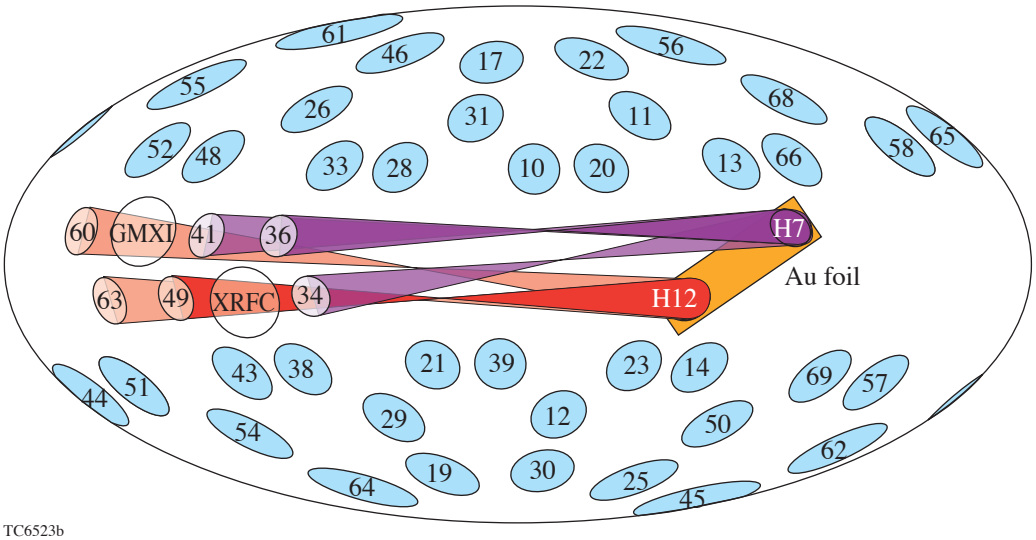

Figure 102.6
Configuration for polar-direct-drive (PDD) experiments on OMEGA. To best approximate the NIF indirect-drive configuration, the target is irradiated with 40 of the 60 OMEGA beams in rings at 21°, 42°, and 59° from the vertical axis of symmetry (top and bottom portions). Some of the other beams at ±9° from the equator (central portion) irradiate a gold backlighter foil, viewed in particular by an x-ray framing camera (XRFC).

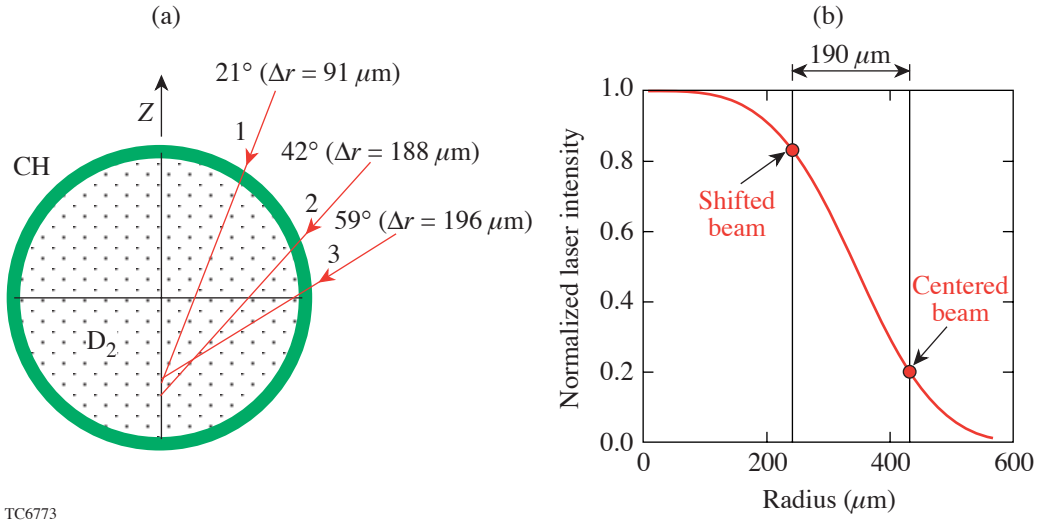

Figure 102.7
(a) Repointings Δr used for the three rings of OMEGA laser beams, measured perpendicular to the beam axes. The capsule is a 20-μm-thick CH shell of 865-μm diameter filled with 15 atm of D_2. (b) Target-plane intensity distribution for an OMEGA beam. The solid circles indicate the intensities and radii of rays that can miss the initial target edge for shifted and centered beams.

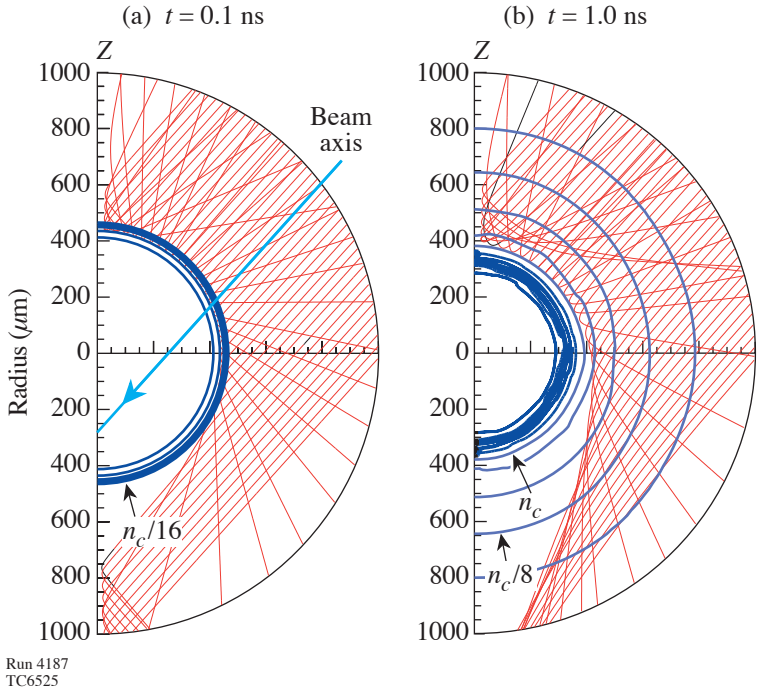

Figure 102.8
Electron-density contours (heavy lines) and a selection of ring-2 ray trajectories in the plane containing the laser axis and the z axis (thin lines), (a) near the start and (b) near the end of the laser pulse. The contour spacing is a factor of 2 in density. The energy loss due to PDD is less than might be expected from Fig. 102.7(b) because of absorption in the expanding plasma.

The time dependence of the predicted absorption is quantified in Fig. 102.9. The incident laser pulse is represented as a 1-ns flat pulse with a linear rise and fall, producing a nominal 16 kJ on target (400 J per beam). The absorbed power rises in time as the coronal scale length increases. The standard-PDD target is predicted to absorb 66% of the incident laser energy, compared with 75% for the 1-D (center-pointed) case. This is roughly equivalent to a 10% incident energy reduction, used when the 1-D code *LILAC* simulates the PDD implosions. The curve labeled "1-D" corresponds to this case and is quite close to the standard-PDD curve.

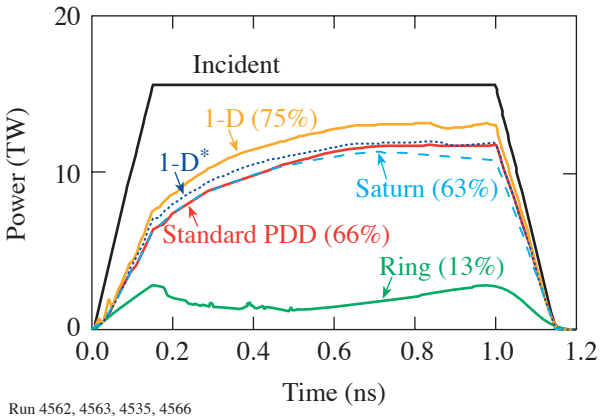

Figure 102.9
Incident and absorbed power as a function of time for several *SAGE* simulations with 16 kJ of incident laser energy, the time-integrated absorption fractions given in parentheses. The curves labeled 1-D are for symmetric irradiation, with 1-D* indicating a 10% reduction of incident energy. For the Saturn simulation, the upper and lower curves apply to the capsule and ring, respectively.

The highly anisotropic distribution of unabsorbed light predicted for PDD makes it difficult to measure the laser absorption using the small number of scattered-light calorimeters on the OMEGA target chamber, as does the material blowoff from the backlighting targets. A separate absorption experiment was carried out to test the modeling of obliquely incident beams. This was done in a symmetric way by taking advantage of the grouping of the OMEGA beams into 12 pentagonal faces of five beams each.[2] Each beam was repointed so that its axis intersected a 1600-μm-diam, solid-CH target at the point where the axis of its first or second nearest neighbor would normally intersect. This is illustrated in the inset to Fig. 102.10 for a single move around the group (corresponding to Δr = 335 μm). Targets were also shot for a double move (Δr = 514 μm). Large targets were used for this experiment to minimize the transmission of laser energy into the opposing beam ports. The absorption fractions determined by a pair of full-aperture backscatter calorimeters, shown in Fig. 102.10, agree very closely with the *SAGE* predictions, providing confidence in the absorption modeling of obliquely incident beams.

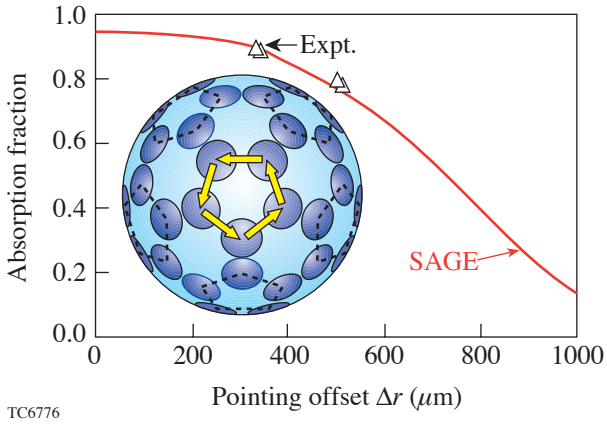

Figure 102.10
Experimental and simulated absorption as a function of pointing offset Δr on large, 1600-μm-diam solid CH targets. Each beam was repointed either one position (as shown in the inset) or two positions around its pentagonal ring on the OMEGA target chamber to allow the effect of oblique incidence to be studied with the minimum loss of uniformity.

Framed x-ray backlighting was the primary diagnostic used for the implosion experiments. A set of four images at 250-ps intervals, integrated over 50-ps frame times, is shown in Fig. 102.11. The framing camera was timed to diagnose the implosion from the end of the laser pulse to ~1 ns later. The first frame, at 1.0 ns (around the end of the laser pulse), showed a ring of coronal self-emission that extended beyond the x-ray emission spot from the gold backlighter foil. This self-emission was also observed by an imaging streak camera. Each of the later images shows a ring of x-ray absorption that becomes smaller as the target implodes. The rings are almost round, indicating that the PDD drive is nearly uniform, but with some low-mode structure analyzed in detail below. The position of the ring relative to the backlighting spot varies due to parallax. Simulations show that, for the first three images, the x-ray absorption minimum is virtually independent of x-ray wavelength in the relevant 2- to 3-keV range and is located very close to the inner surface of the imploding shell, whereas the self-emission ring comes from the corona on the outside of the target. (The fourth image is harder to interpret since it depends on the profiles near stagnation.)

Experimental determinations of the average shell radius as a function of time are shown in Fig. 102.12. The imaging streak camera provided data up to the end of the laser pulse. The average radii from framing-camera images were available through most of the implosion (although not up to peak compression). The horizontal error bars on these data points indicate the timing uncertainty and the vertical error bars represent the accuracy with which the shell radius can be determined. The experimental data were simulated in 1-D by *LILAC* (postprocessed using Spect3D[19]) and *SAGE*, both codes using a flux limiter[20] f of 0.06. The lowest-order shell motion is modeled well by both codes, with a small timing difference evident with respect to the framing-camera data.

The main result of the experiment is provided by the solid points and curves of Fig. 102.13, which gives the x-ray absorption radius R_{abs} as a function of θ at two successive times during the early stages of the implosion [corresponding to Figs. 102.11(b) and 102.11(c)]. To obtain $R_{abs}(\theta)$, the positions of the absorption maximum at points around the ring were visually determined, a circle was fit through these positions,

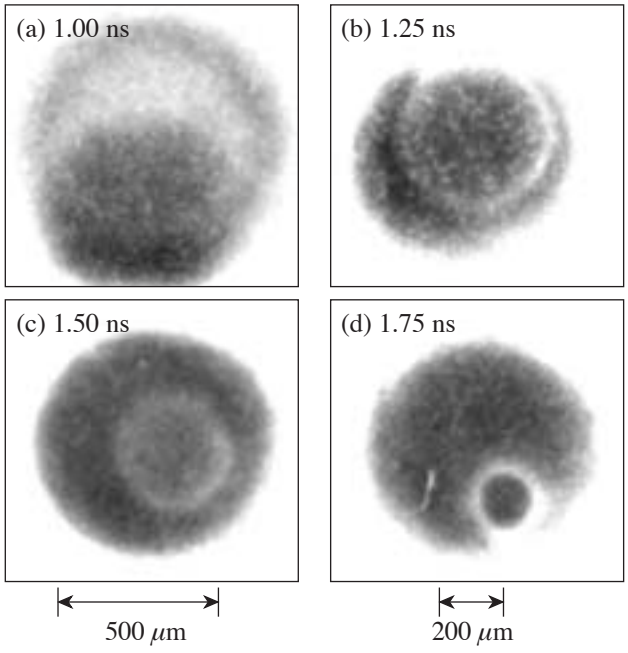

Figure 102.11
A sequence of four backlit x-ray images at successive times. The first image (at the end of the laser pulse) shows a ring due to self-emission from the corona. The following images show distinct rings of x-ray absorption, corresponding roughly to the inner edge of the imploding CH shell.

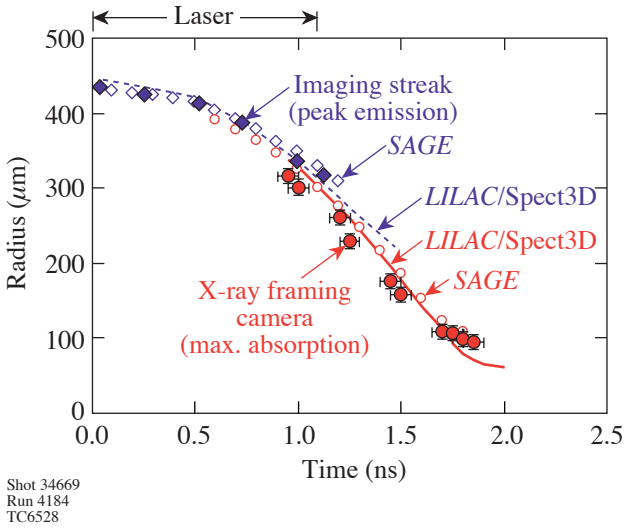

Figure 102.12
Measured and simulated trajectory of the imploding CH shell. The radius of maximum self-emission from the imaging streak camera (solid diamonds) is compared with *SAGE* predictions (open diamonds) and predictions from *LILAC* postprocessed by Spect3D (dotted line). The radius of maximum x-ray absorption (solid circles) is compared with *SAGE* (open circles) and *LILAC*/Spect3D (solid line). Both simulations assume 1-D symmetric irradiation with the incident laser energy reduced by 10%.

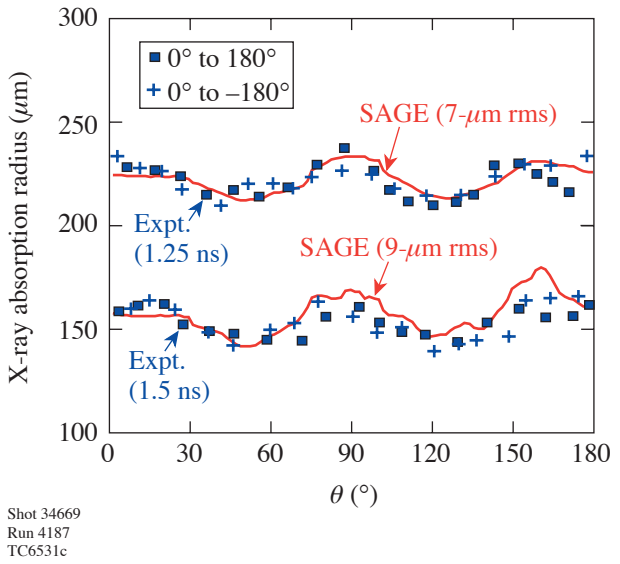

Figure 102.13
Experimental radii of maximum x-ray absorption R_{abs} obtained from the framing-camera images of Fig. 102.11 at 1.25 and 1.5 ns, plotted as a function of angle from the vertical. Squares (plusses) indicate clockwise (counterclockwise) scans from the top of the images. The solid lines are the *SAGE* predictions of R_{abs} based on the calculated center-of-mass location R_{cm}, with minor adjustments for the viewing angle and the difference between R_{cm} and R_{abs}.

and the center of this circle was used as a reference point. No corrections were made for nonuniformities in the backlighter. The different symbols in Fig. 102.13 correspond to scanning around the images from top to bottom in the two angular directions. These are equivalent for an azimuthally symmetric implosion; the good agreement is consistent with good azimuthal symmetry and also indicates that errors associated with nonuniformities in the backlighter are minimal. The calculated curves are based on the center-of-mass radius R_{cm} of the imploding shell, adjusted by estimates of the distance to the x-ray minimum (14 μm at 1.25 ns and 24 μm at 1.5 ns). This method proved more robust than direct comparison with the calculated x-ray minimum, whose exact location was subject to some numerical noise. The calculated curves are taken at times (0.15 ns later than the nominal experimental times) that allow comparison to be made of the θ variations at the same values of the average shell radius. The 0.15-ns offset represents a combination of the experimental timing uncertainty and the observation that the agreement between simulation and experiment for the lowest-order shell motion (Fig. 102.12), while very close, is not exact. Deviations from symmetry about θ = 90° in the simulations, in particular the peak at 160° at the later time, are due to numerical noise that grows at later times. The best indication of the PDD drive nonuniformity is provided at the earlier time when the noise is small.

Figure 102.13 shows that the rms perturbation amplitude increased from 7 μm to 9 μm as the shell radius decreased from ~225 μm to ~150 μm (compared with an initial radius of ~430 μm). At both times the experimental mode structure and amplitude agree well with the simulations, with the drive weak at the equator and at the poles. This agreement provides confidence that the beam pointings for optimum uniformity can be accurately predicted. This is important for the NIF, where a limited number of shots will be available for tuning the drive uniformity.

The compressed core was imaged using a time-integrating Kirkpatrick–Baez (KB) microscope with ~3-μm spatial resolution, filtered to look at x rays from 3 to 7 keV.[21] Shot 34644 (60 beams, each with 2/3 of the nominal beam energy of 400 J pointed to target chamber center) and shot 34668 (40 PDD beams) are compared in Figs. 102.14(a) and 102.14(b). The core in the PDD case was less spherical, and the neutron yield Y_{DD} was reduced by a factor of about 3.

The evolution of the shell nonuniformity observed in Fig. 102.13 was consistent with the center-of-mass velocity nonuniformity at the end of the laser pulse (1.1 ns), shown in

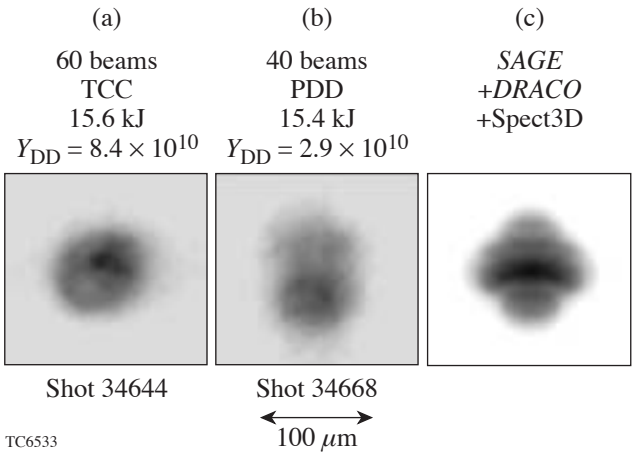

Figure 102.14
Time-integrated KB microscope images for (a) a target irradiated symmetrically with 60 beams, each with 2/3 nominal energy, pointed at target chamber center (TCC), (b) a 40-beam PDD target, and (c) a simulation of (b). While all images share the same spatial scale, care should be exercised when comparing (b) and (c) because of the different gray scales used.

Fig. 102.15(a). The minimum at the equator (and, indeed, the falloff from θ = 60° to θ = 90°) is found for all feasible combinations of ring pointings. The optimum overall rms nonuniformity of 3.8% is obtained by reducing the drive at the poles. The low drive pressure at the equator causes mass to flow toward the equator. Figure 102.15(b) shows the transverse velocity V_θ, positive between θ = 60° and θ = 90° and negative from 90° to 120°. This small velocity (whose rms is ~2.5% of V_r) can lead to increasing transverse mass flow toward the equator as the implosion proceeds.

To follow the implosion from the end of the laser pulse, low-ℓ fits to the *SAGE* center of mass V_r and V_θ were used to perturb a hitherto uniform *DRACO* simulation. Even values of ℓ were used for V_r and odd for V_θ (as V_θ results from gradients in the θ direction). *DRACO* contours of mass density ρ and electron temperature T_e at the time of peak neutron production are given in Figs. 102.15(c) and 102.15(d), respectively. The solid line indicates the CH/D_2 interface. The ℓ = 4 perturbation continues throughout the implosion. The calculated neutron yield was 5.4×10^{10}, reduced from 1.3×10^{11} for a comparison unperturbed simulation by a factor of 0.42, close to the experimental reduction factor of 0.35, suggesting that the experimental reduction can be explained mainly by the imposed low-ℓ perturbations. (Similar yield reductions have been obtained in full *DRACO* simulations using its approximate ray-trace option.)

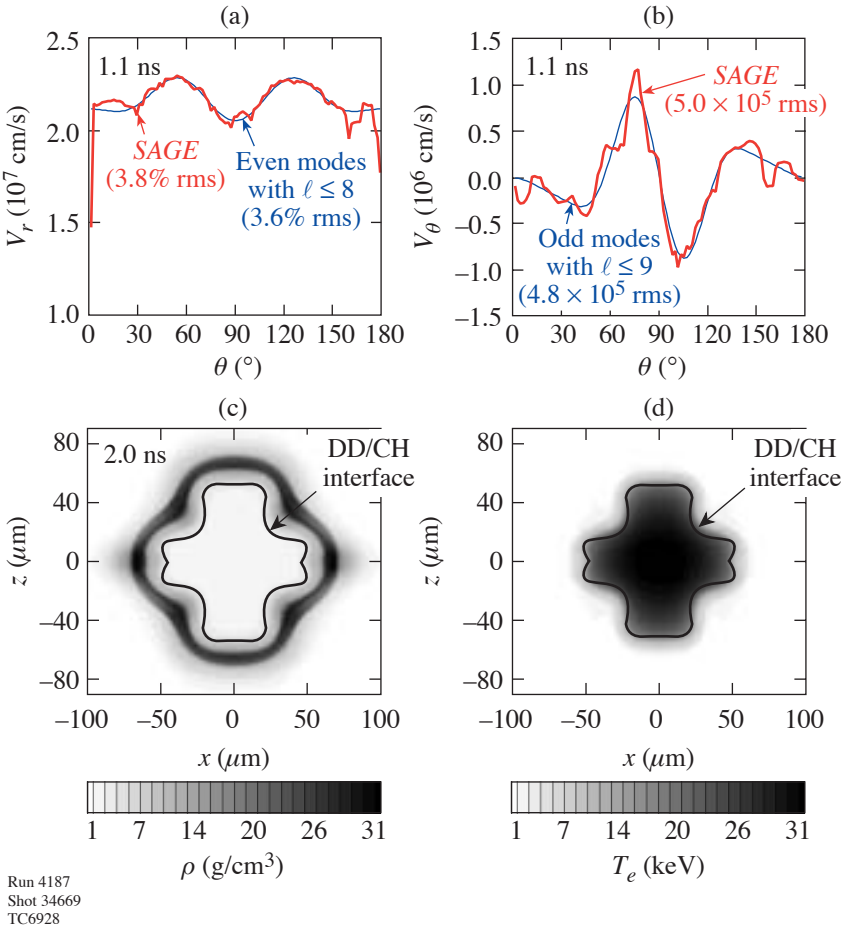

Figure 102.15
SAGE/*DRACO* simulation of a PDD implosion. Low-ℓ Legendre fits to (a) the center-of-mass radial velocity V_r and (b) the transverse velocity V_θ calculated by *SAGE* at the end of the laser pulse (1.1 ns) were used to perturb a hitherto symmetric *DRACO* simulation. The density ρ and electron temperature T_e contours at the time of peak neutron production are given in (c) and (d), respectively.

The *DRACO* profiles were postprocessed by Spect3D to form the time-integrated x-ray image shown in Fig. 102.14(c). The experimental image shows a lower intensity in the upper half as indicated in the calculated image. This is ascribed to mass that has accumulated near the equator, partially obstructing the view of the core taken from 15.6° below the equator.[22]

Saturn Experiments on OMEGA

The first Saturn target implosion experiments have been performed on OMEGA. Standard OMEGA capsules (20-μm CH shells filled with 15 atm of D_2) were supported using spider silk on a CH ring of 1100-μm major radius and 150-μm minor radius (see Fig. 102.16). The capsule was centered in the ring to an accuracy usually better than 40 μm. While the calculated optimum pointing called for the ring-1 Δr to be changed from 90 μm to 30 μm, to give a stronger drive at the poles, the actual experimental pointing was unchanged to isolate the change of uniformity induced by the ring.[23] The backlighting configuration was modified from that shown in Fig. 102.6 to include a second framing camera viewing from 26.6° above the equator, to avoid obscuration by the ring.

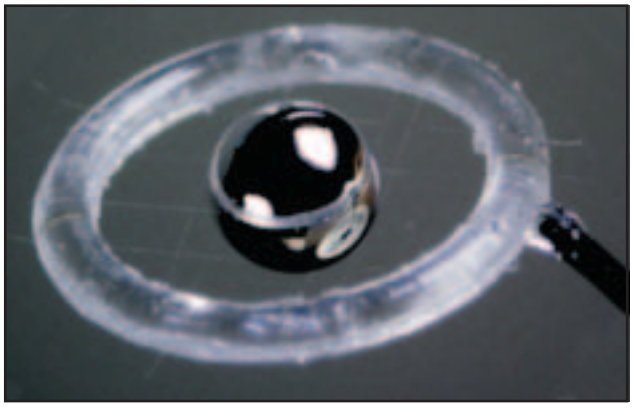

Figure 102.16
A Saturn target shot on OMEGA. Using eight strands of spider silk, a standard 865-μm-diam capsule is mounted on a CH ring of major radius 1100 μm and minor radius 150 μm.

The ring plasma forms mainly in the later part of the laser pulse, as in the NIF design described in the preceding article. Predicted density contours at two times are shown in Fig. 102.17. A "bow shock" is observed where the ring plasma and capsule plasma collide. The absorbed power in the capsule was almost the same as in the standard-PDD case (see Fig. 102.9) and that in the ring was fairly constant.

Figure 102.18(a) shows a time-integrated pinhole-camera image of the target, viewed 10.8° above the equator. The ring appears as a shadow obscuring some of the plasma. There is evidence of the bow shock near the inner edge of the ring. The imploded core is heavily overexposed. A better-filtered image of the core, obtained from the KB microscope and dominated by emission from the CH/D_2 interface, shows prolate core emission [Fig. 102.18(b)].

Framing-camera images of the imploding shell obtained from the 26.6° view [Figs. 102.18(c)–102.18(e)] show a clear $\ell = 2$ mode, evident from the earliest time. The x-ray absorption radii from the first two images, whose times correspond to the standard-PDD data shown in Fig. 102.13, are plotted in Fig. 102.19 along with predictions corrected for the viewing angle (i.e., around a great circle in a plane tipped 26.6° from the vertical). The predictions (solid curves) show an $\ell = 4$ pattern with slightly reduced amplitude compared with the standard-PDD case (dotted curves). The Saturn data show an $\ell = 2$ mode with the strongest drive on the equator, larger than predicted.

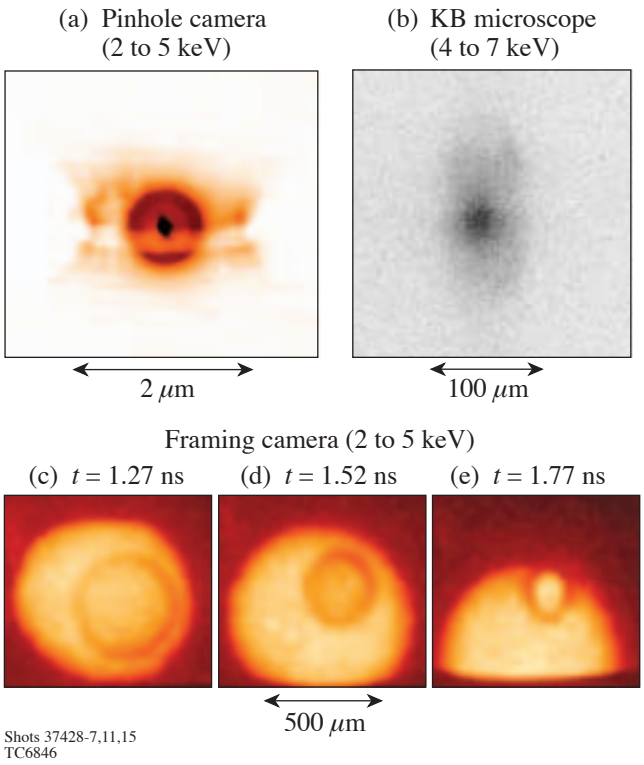

Figure 102.18
X-ray images of Saturn-target implosions. (a) Time-integrated pinhole-camera image, from 10.8° above the equator, including self-emission, the shadow of the ring, the bow shock, and a prolate core (saturated). (b) Time-integrated KB microscope image of the core. (c)–(e) Framing-camera backlit images of the imploding shell viewed 26.6° above the equator.

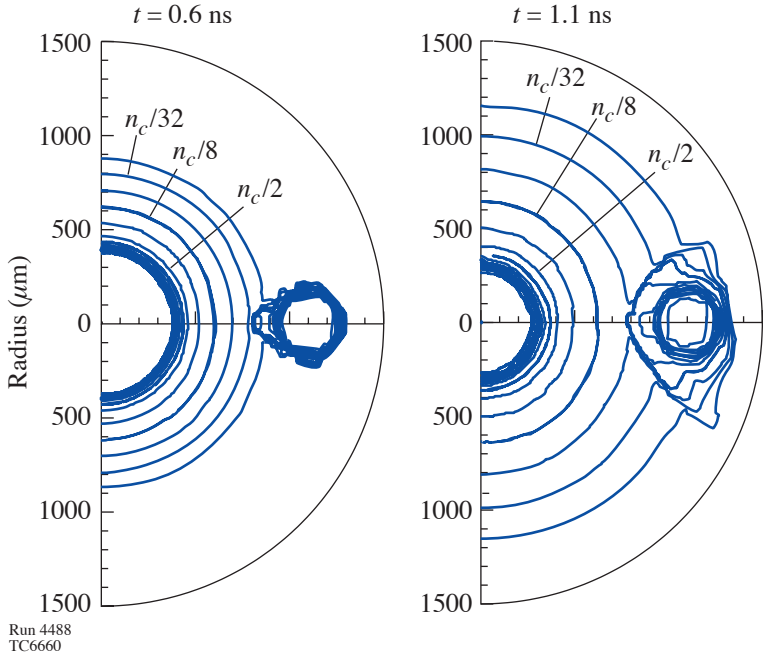

Figure 102.17
Simulated electron-density contours at 0.6 and 1.1 ns for the Saturn target. The ring plasma grows primarily in the second half of the laser pulse, forming a "bow shock" where it collides with the plasma ablating from the capsule.

The primary reason for this disagreement is believed to be radiation from the ring plasma to the capsule, not included in the simulations. In addition, it is possible that the ring plasma is not behaving as modeled. Much of the laser energy absorbed by the ring comes from rays near the edge of the beam profile, which may contain more energy than implied by the super-Gaussian fit. The ring may not be azimuthally symmetric: while it is probably irradiated uniformly by the light from all beams that is refracted from the capsule plasma, it is also irradiated directly in localized regions by the edges of the ring-3 beams. Such asymmetries would lead to a more rapid local growth of the ring plasma.

The Saturn target that came closest to design specifications yielded 1.8×10^{10} DD neutrons, slightly less than two standard-PDD targets shot immediately prior to the Saturn targets that yielded 2.1 and 2.4×10^{10} neutrons, respectively. This is consistent with the greater low-ℓ drive variations seen in Fig. 102.19, suggesting that removal of the strong $\ell = 2$ nonuniformity would improve the Saturn yield. This can be accomplished by changing some of the repointings Δr to shift some of the drive back toward the poles or by increasing the major radius (or decreasing the minor radius) of the ring.

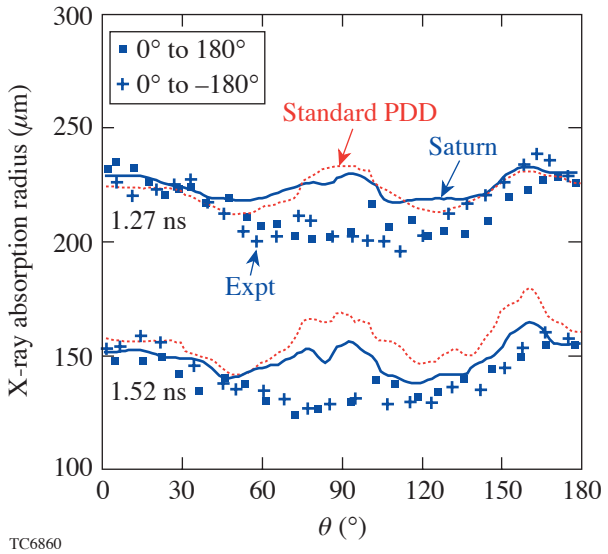

Figure 102.19
X-ray absorption radius as a function of angle θ around the image obtained from the 1.27-ns and 1.52-ns Saturn-target images in Fig. 102.18 together with *SAGE* predictions obtained as in Fig. 102.13 (solid curves). The dotted curves are taken from Fig. 102.13 for a standard-PDD target. The experimental data indicate that the increase in equatorial capsule drive is greater than predicted.

High-Gain Saturn Design for the NIF

In the preceding article, a Saturn design for the NIF was calculated up to the end of the laser pulse and optimized for minimum rms center-of-mass nonuniformity. In this section the subsequent implosion of this design is modeled using the *SAGE*/*DRACO* technique described above.

The Saturn ignition design adds a CH ring of 3000-μm major radius to the all-DT capsule described in Ref. 7 and repoints the beams incident at 30°, 44.5°, and 50° with Δr = 240 μm, 280 μm, and 750 μm, respectively. The 44.5° and 50° beams use "elliptical" phase plates whose target-plane profiles are reduced in the z direction by factors of cos(30°) and cos(50°), respectively. The center-of-mass velocity perturbations V_r and V_θ near the end of the laser pulse are shown in Figs. 102.20(a) and 102.20(b), together with low-mode Legendre fits. Of the 1.3% calculated rms V_r perturbation, 1.1% can be accounted for by modes 2 and 4 (the difference largely being due to noise in the simulation). An initially symmetric *DRACO* simulation was perturbed with the Legendre fits and was continued through the thermonuclear burn phase. (More-accurate simulations would also transfer the 9-μm-rms center-of-mass modulations in shell excursion at this time and modulations in mass per solid angle, both considered to be small.) Contours of density and ion temperature from *DRACO* are shown in Figs. 102.20(c) and 102.20(d) at the onset of ignition. The imposed ℓ-mode pattern is maintained through the coasting and deceleration stages. This nonuniformity is sufficiently small to allow ignition to occur, with little effect on the propagating burn wave. The resulting gain is 38, close to the 1-D gain of 45. This result is consistent with the work of McKenty *et al.*,[7] who found that low-ℓ perturbations have less effect on the gain of the all-DT design than higher-ℓ perturbations ($\ell \gtrsim 10$) of the same amplitude. Consistently, other *SAGE*/*DRACO* calculations with similar rms nonuniformities imposed in higher-ℓ modes (~8) perform less well. Inner-ice roughness and imprint, not included in the simulation presented here, are likely to result in similar (~30%) reductions in yield as for symmetrically driven capsules.[7]

Conclusions

Experiments on OMEGA have confirmed that reasonably symmetric implosions can be carried out using 40 of the 60 beams in a polar configuration. Further, the drive perturbations can be diagnosed with amplitudes and mode structure that are in good agreement with simulations.

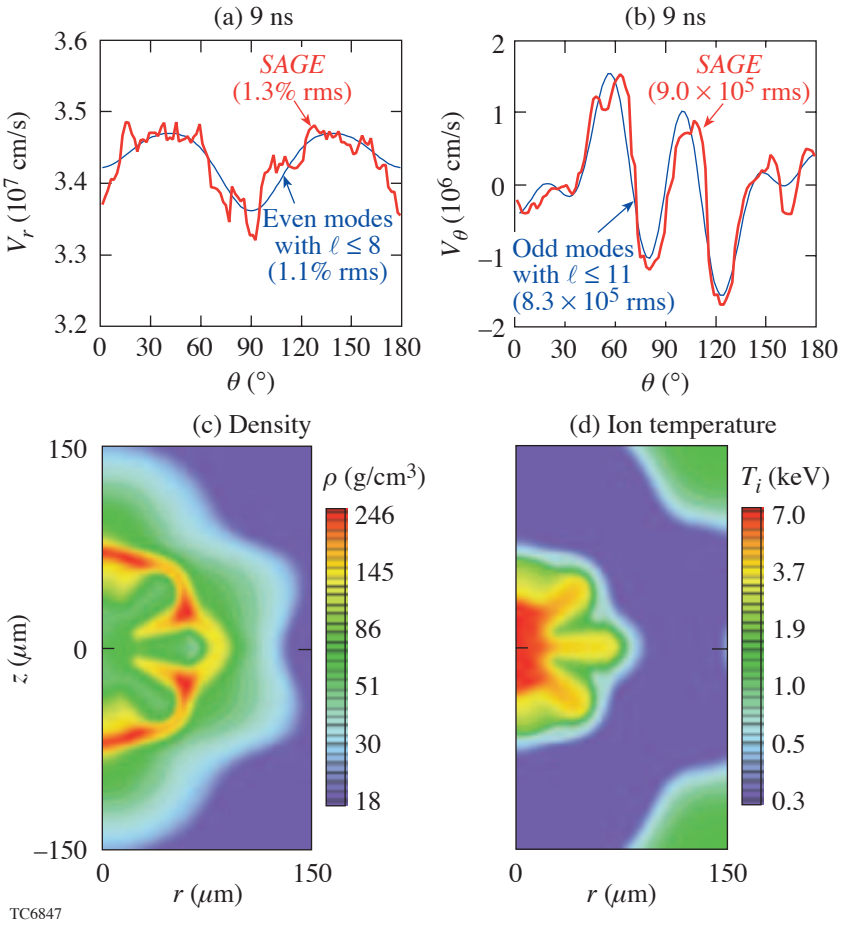

Figure 102.20
SAGE/*DRACO* simulation of the NIF Saturn target. Low-ℓ fits to (a) the *SAGE*-calculated center-of-mass radial velocity V_r and (b) the transverse velocity V_θ were used to perturb a symmetric *DRACO* simulation. The density ρ and ion temperature T_i contours at the time of ignition are given in (c) and (d), respectively. The gain of 38 is close to 1-D.

The Saturn implosions reported here demonstrated that a low-*Z* ring can be used to increase the drive on the equator. Indeed, the maximum drive was observed at the equator, which, according to calculations, cannot happen for standard-PDD targets on the OMEGA laser system. The prospects for improving the uniformity of Saturn targets are excellent, with the possibilities including changes to the beam pointings and ring dimensions. Subsequent OMEGA experiments and modeling, to be reported in a future issue of the LLE Review, have shown that the implosion symmetry and yield can be improved by readjusting the beam pointings and that radiation is indeed the primary cause of the discrepancy between experiment and simulations. Further experiments will provide a better understanding of the formation and evolution of the ring plasma and its azimuthal symmetry, and the physics of the bow shock and its contribution to x-ray emission from the ring remains to be explored. These experiments will enable more-accurate calculations to be made of Saturn targets for the NIF.

Hydrodynamic modeling of the standard-PDD experiments using a combination of *SAGE* and *DRACO* led to a yield reduction close to that observed experimentally. Similar modeling was applied to the Saturn design for the NIF and led to a predicted gain close to 1-D. This result is very encouraging since it improves the prospects of obtaining direct-drive ignition and high gain on the NIF many years before conversion of the NIF to the direct-drive configuration. This work will be published in Ref. 24.

ACKNOWLEDGMENT

The authors are grateful to Dr. David Meyerhofer for a careful review of the manuscript and many helpful suggestions. This work was supported by the U.S. Department of Energy Office of Inertial Confinement Fusion under Cooperative Agreement No. DE-FC52-92SF19460, the University of Rochester, and the New York State Energy Research and Development Authority. The support of DOE does not constitute an endorsement by DOE of the views expressed in this article.

REFERENCES

1. E. M. Campbell and W. J. Hogan, Plasma Phys. Control. Fusion **41**, B39 (1999).
2. S. Skupsky, J. A. Marozas, R. S. Craxton, R. Betti, T. J. B. Collins, J. A. Delettrez, V. N. Goncharov, P. W. McKenty, P. B. Radha, T. R. Boehly, J. P. Knauer, F. J. Marshall, D. R. Harding, J. D. Kilkenny, D. D. Meyerhofer, T. C. Sangster, and R. L. McCrory, Phys. Plasmas **11**, 2763 (2004).
3. J. D. Kilkenny, Laboratory for Laser Energetics, private communication (2002).
4. R. S. Craxton, presented at the 33rd Anomalous Absorption Conference, Lake Placid, NY, 22–27 June 2003 (Paper WO3).
5. R. S. Craxton, Bull. Am. Phys. Soc. **48**, 56 (2003).
6. C. P. Verdon, Bull. Am. Phys. Soc. **38**, 2010 (1993).
7. P. W. McKenty, V. N. Goncharov, R. P. J. Town, S. Skupsky, R. Betti, and R. L. McCrory, Phys. Plasmas **8**, 2315 (2001).
8. R. S. Craxton and R. L. McCrory, J. Appl. Phys. **56**, 108 (1984).
9. P. B. Radha, T. J. B. Collins, J. A. Delettrez, D. Keller, P. W. McKenty, and R. P. J. Town, presented at the 30th Annual Anomalous Absorption Conference, Ocean City, MD, 21–26 May 2000 (Paper 2P11).
10. P. B. Radha, V. N. Goncharov, T. J. B. Collins, J. A. Delettrez, Y. Elbaz, V. Yu. Glebov, R. L. Keck, D. E. Keller, J. P. Knauer, J. A. Marozas, F. J. Marshall, P. W. McKenty, D. D. Meyerhofer, S. P. Regan, T. C. Sangster, D. Shvarts, S. Skupsky, Y. Srebro, R. P. J. Town, and C. Stoeckl, Phys. Plasmas **12**, 032702 (2005).
11. S. Skupsky, R. Betti, T. J. B. Collins, V. N. Goncharov, D. R. Harding, R. L. McCrory, P. W. McKenty, D. D. Meyerhofer, and R. P. J. Town, in *Inertial Fusion Sciences and Applications 2001*, edited by K. Tanaka, D. D. Meyerhofer, and J. Meyer-ter-Vehn (Elsevier, Paris, 2002), pp. 240–245.
12. D. Eimerl, ed., Lawrence Livermore National Laboratory, Livermore, CA, UCRL-ID-120758 (1995).
13. S. G. Gledinning, Lawrence Livermore National Laboratory, private communication (2003).
14. G. A. Kyrala *et al.*, Laser Part. Beams **23**, 207 (2005).
15. F. J. Marshall, J. A. Delettrez, R. Epstein, R. Forties, R. L. Keck, J. H. Kelly, P. W. McKenty, S. P. Regan, and L. J. Waxer, Phys. Plasmas **11**, 251 (2004).
16. S. Skupsky and R. S. Craxton, Phys. Plasmas **6**, 2157 (1999).
17. T. R. Boehly, V. A. Smalyuk, D. D. Meyerhofer, J. P. Knauer, D. K. Bradley, R. S. Craxton, M. J. Guardalben, S. Skupsky, and T. J. Kessler, J. Appl. Phys. **85**, 3444 (1999).
18. F. J. Marshall, J. A. Delettrez, R. Epstein, R. Forties, V. Yu. Glebov, J. H. Kelly, T. J. Kessler, J. P. Knauer, P. W. McKenty, S. P. Regan, V. A. Smalyuk, C. Stoeckl, J. A. Frenje, C. K. Li, R. D. Petrasso, and F. H. Séguin, Bull. Am. Phys. Soc. **48**, 56 (2003).
19. Prism Computational Sciences, Inc., Madison, WI, Report No. PCS-R-041, Ver. 3.0 (2002). See also J. J. MacFarlane *et al.*, in *Inertial Fusion Sciences and Applications 2003*, edited by B. A. Hammel, D. D. Meyerhofer, J. Meyer-ter-Vehn, and H. Azechi (American Nuclear Society, La Grange Park, IL, 2004), pp. 457–460.
20. R. C. Malone, R. L. McCrory, and R. L. Morse, Phys. Rev. Lett. **34**, 721 (1975).
21. M. C. Richardson, P. W. McKenty, F. J. Marshall, C. P. Verdon, J. M. Soures, R. L. McCrory, O. Barnouin, R. S. Craxton, J. Delettrez, R. L. Hutchison, P. A. Jaanimagi, R. Keck, T. Kessler, H. Kim, S. A. Letzring, D. M. Roback, W. Seka, S. Skupsky, B. Yaakobi, S. M. Lane, and S. Prussin, in *Laser Interaction and Related Plasma Phenomena*, edited by H. Hora and G. H. Miley (Plenum Publishing, New York, 1986), Vol. 7, pp. 421–448.
21. F. J. Marshall and Q. Su, Rev. Sci. Instrum. **66**, 725 (1995).
22. R. Epstein, R. S. Craxton, J. A. Delettrez, F. J. Marshall, J. A. Marozas, P. W. McKenty, P. B. Radha, and V. A. Smalyuk, Bull. Am. Phys. Soc **49**, 180 (2004).
23. The second series of standard-PDD experiments and the Saturn targets used $\Delta r = 90\ \mu$m, 180 μm, and 180 μm for rings 1–3, respectively, not significantly different from the values for the first series indicated in Fig. 102.7.
24. R. S. Craxton, F. J. Marshall, M. Bonino, R. Epstein, P. W. McKenty, S. Skupsky, J. Delettrez, I. V. Igumenshchev, D. W. Jacobs-Perkins, J. P. Knauer, J. A. Marozas, P. B. Radha, and W. Seka, "Polar Direct Drive—Proof-of-Principle Experiments on OMEGA and Prospects for Ignition on the NIF," to be published in Physics of Plasmas.